Exploring Oxygen Activity in the High Energy P2-Type Na$_{0.78}$Ni$_{0.23}$Mn$_{0.69}$O$_2$ Cathode Material for Na-Ion Batteries

Chuze Ma,[†] Judith Alvarado,[†] Jing Xu,[‡,§] Raphaële J. Clément,[∥,⊥] Moses Kodur,[†] Wei Tong,[‡] Clare P. Grey,*[,∥] and Ying Shirley Meng*[,†]

[†]Department of NanoEngineering, University of California San Diego, La Jolla, California 92037, United States
[‡]Energy Storage and Distributed Resources Division, Lawrence Berkeley National Laboratory, Berkeley, California 94720, United States
[§]Department of Materials Science and Engineering, Iowa State University, Ames, Iowa 50011, United States
[∥]Department of Chemistry, University of Cambridge, Lensfield Road, Cambridge CB2 1EW, United Kingdom
[⊥]Department of Materials Science and Engineering, University of California Berkeley, Hearst Mining Memorial Building, Berkeley, California 94720, United States

Ⓢ *Supporting Information*

ABSTRACT: Large-scale electric energy storage is fundamental to the use of renewable energy. Recently, research and development efforts on room-temperature sodium-ion batteries (NIBs) have been revitalized, as NIBs are considered promising, low-cost alternatives to the current Li-ion battery technology for large-scale applications. Herein, we introduce a novel layered oxide cathode material, Na$_{0.78}$Ni$_{0.23}$Mn$_{0.69}$O$_2$. This new compound provides a high reversible capacity of 138 mAh g^{-1} and an average potential of 3.25 V vs Na$^+$/Na with a single smooth voltage profile. Its remarkable rate and cycling performances are attributed to the elimination of the P2−O2 phase transition upon cycling to 4.5 V. The first charge process yields an abnormally excess capacity, which has yet to be observed in other P2 layered oxides. Metal K-edge XANES results show that the major charge compensation at the metal site during Na-ion deintercalation is achieved via the oxidation of nickel (Ni^{2+}) ions, whereas, to a large extent, manganese (Mn) ions remain in their Mn^{4+} state. Interestingly, electron energy loss spectroscopy (EELS) and soft X-ray absorption spectroscopy (sXAS) results reveal differences in electronic structures in the bulk and at the surface of electrochemically cycled particles. At the surface, transition metal ions (TM ions) are in a lower valence state than in the bulk, and the O K-edge prepeak disappears. On the basis of previous reports on related Li-excess LIB cathodes, it is proposed that part of the charge compensation mechanism during the first cycle takes place at the lattice oxygen site, resulting in a surface to bulk transition metal gradient. We believe that by optimizing and controlling oxygen activity, Na layered oxide materials with higher capacities can be designed.
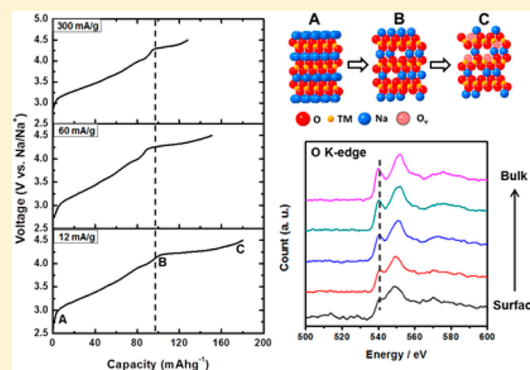
1. INTRODUCTION

The effective use of renewable energy is one of the most important issues that needs to be addressed to achieve a sustainable society.[1] Renewable energy sources such as solar and wind energy do not produce electricity in a consistent manner; thus, a large-scale energy storage system is required to integrate the intermittent energy into a stable power supply that can meet consumption in real time. High-energy Li-ion batteries (LIBs) are expected to contribute to the solution; however, the expected increase in the cost of raw lithium, as compared to abundant and low-cost Na, has led to a resurgence of interest in room-temperature Na-ion batteries (NIBs) as potential, cheaper alternatives for large-scale applications. Furthermore, rechargeable NIBs share many similarities with LIBs, and thus state-of-the-art LIB technologies can provide some direction and speed progress in NIB research.

The easy synthesis of layered transition metal oxides, Na$_x$TMO$_2$ (0 < x < 1 and TM = transition metals), and their promising electrochemical properties, have resulted in a large number of recent reports on this family of NIB cathode materials.[2−15] In Na$_x$TMO$_2$, TM ions reside within layers of edge sharing metal-oxide (TMO$_6$) octahedra, while Na ions are accommodated between the layers. The most common structures are O3- and P2-type, according to a classification devised by Delmas et al., where Na ions occupy octahedral (O) and trigonal prismatic (P) sites, respectively.[16] The number following the sodium coordination environment describes the number of TMO$_2$ layers in the unit cell. P2 and O3 structures differ in their oxygen stacking sequence, ABCABC stacking for
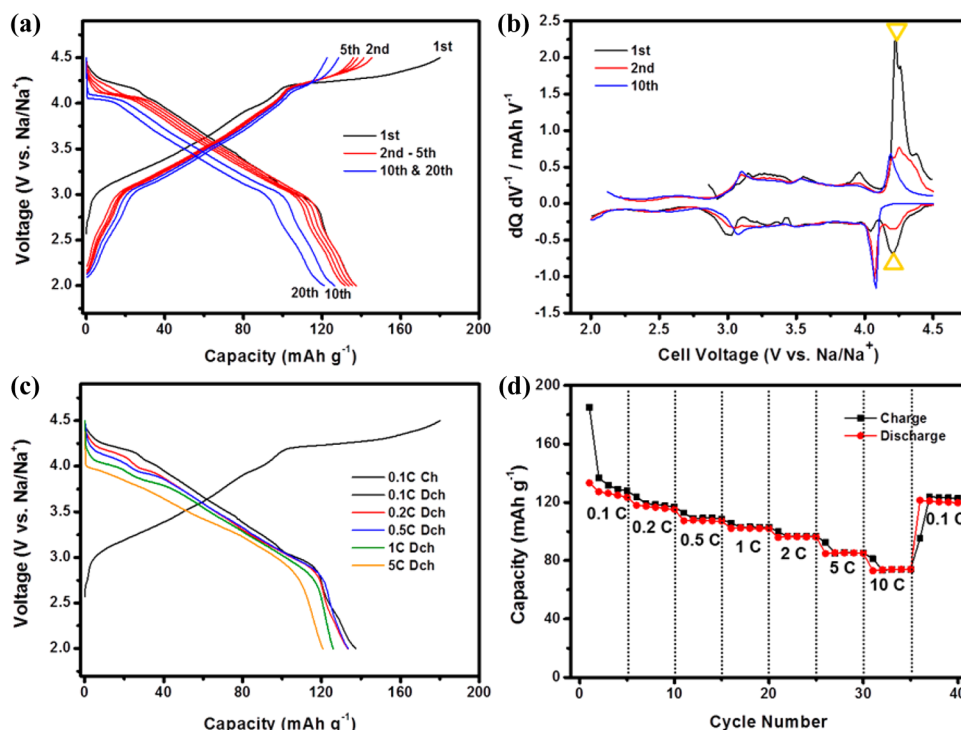
Figure 1. Electrochemical characterization of $Na_{0.78}Ni_{0.23}Mn_{0.69}O_2$: (a) Electrochemical profiles during the first, second, third, fourth, fifth, 10th, and 20th cycles at 0.1 C, (b) differential capacity ($dQ\ dV^{-1}$) versus voltage plots at various cycles, (c) voltage profiles at different current densities, and (d) rate and cycling capabilities at different current densities from 0.1 to 10 C (1 C = 121 mA g^{-1}).

O3 and ABBA stacking for P2, leading to different electrochemical characteristics. On the one hand, O3-type materials are less structurally reversible when cycled above 4.0 V. Their rate performance is also lower because Na ions need to diffuse through face-shared interstitial tetrahedral sites.[17,18] On the other hand, P2-type materials, as synthesized, contain Na-vacancies in the Na layers. Thus, when cycled versus an Na metal anode (large Na-excess), an apparent first cycle Coulombic efficiency of above 100% results, the discharged material containing fewer Na-vacancies. The large fraction of these unoccupied Na^+ ion sites in as-synthesized P2 materials leads to problems in terms of electrode balancing in full cells.[19] Moreover, P2-type materials undergo phase transitions at high voltage that result in shortened cycle life and poor rate capability.[20,21] Two approaches have been used to alleviate this issue, the first one being to limit the high voltage cutoff to 4.1 V to avoid the P2−O2 transition. In $Na_xMn_{2/3}Ni_{1/3}O_2$, this leads to an increase in capacity retention from 64% to over 95% after 10 cycles.[20] The second approach is to substitute Ni for an electrochemically inactive element, such as Li, to delay structural transitions at higher voltages. Li doping in this family of materials was first explored by Johnson and co-workers, who showed that the P2−$Na_{1.0}Li_{0.2}Ni_{0.25}Mn_{0.75}O_2$ cathode material displays a single smooth voltage profile up to 4.2 V, and excellent cycling and rate capabilities.[22] A following study from our group demonstrated that the Li-doped P2−$Na_{0.80}Li_{0.12}Ni_{0.22}Mn_{0.66}O_2$ maintains its structure up to 4.4 V and exhibits more than 95% of its initial capacity after 50 cycles.[23] The study determined that the presence of monovalent Li ions in the TM layers allows more Na ions to reside in the prismatic sites in the as-prepared material and upon charge. Thus, the phase transformation is delayed upon Na deintercalation, the P2 structure is retained in the high voltage region, and the cycling performance is improved.

Despite a large number of recent studies on various Na layered oxide cathodes with different TM compositions, as discussed in a recent review paper,[24] there was rarely report on the redox activity of oxygen anions in NIB cathode materials. It is now widely accepted that the participation of both metal and oxygen ions in the redox reaction mechanism leads to high energy density in Li-excess LIB cathode materials.[25−30] This topic is of great relevance to the NIB community, as oxygen participation in the high voltage redox reactions could open new perspectives for the design of high energy NIB cathodes. Only very few recent studies on Na_xTMO_2 materials have suggested the participation of oxide ions in the redox processes takes place upon Na electrochemical extraction, for example, in P2−$Na_xM_yMn_{1-y}O_2$ (M = Li, Mg) cathode materials,[31−33] and apart from Yamada and co-workers' work on $E(Ni^{3+}/Ni^{2+}) > E(Ni^{4+}/Ni^{3+})$ redox potential paradox,[34] little experimental evidence has been provided to confirm the contribution of O-based charge compensation phenomena to the observed capacity of the Na positive electrodes. Despite it is proposed that reversible O^{2-}/O^- redox can contribute to the extra capacity in ordered Na_2RuO_3 material,[35,36] the orbitals hybridization and electronic structures between the 4d Ru and O are significantly different from the commonly used 3d TMs, making the findings less representative. Inspired by previous work by Dahn et al., who showed that metal vacancies can facilitate oxygen atom reactivity in cathode materials,[37] we modified the stoichiometry of P2−$Na_xNi_yMn_zO_2$ to design a high Na content, TM-deficient, P2−$Na_{0.78}Ni_{0.23}Mn_{0.69}O_2$ compound. While the large Na-ion reservoir is expected to stabilize the P2 structure up to high voltage, the TM deficiency is expected to activate the oxygen anion redox in the Na layered oxide. The stoichiometry of the compound, $Na_{0.75}Ni_{0.24}Mn_{0.69}O_{1.99}$ (normalized to Mn), was determined

by inductively coupled plasma-optical emission spectroscopy (ICP-OES) and confirmed by Ni/Mn K-edge XAS.

Herein, we report on the synthesis and characterization of the novel layered oxide $Na_{0.78}Ni_{0.23}Mn_{0.69}O_2$. This material consists of a single P2 phase and performs very well as a high energy density rechargeable NIB cathode. The abnormally high capacity observed on first charge is thoroughly investigated. Long-range and short-range structural changes are monitored using ex situ XRD and solid-state nuclear magnetic resonance (ssNMR). The participation of oxygen anions in the initial charge compensation mechanism is explored using EELS and XAS techniques.

2. RESULTS AND DISCUSSION

2.1. Electrochemical Properties of $Na_{0.78}Ni_{0.23}Mn_{0.69}O_2$.
The morphology of the as-synthesized $Na_{0.78}Ni_{0.23}Mn_{0.69}O_2$ particles was characterized by scanning electron microscopy (SEM), as shown in Figure S1. The primary particle size is around 3 μm. Electrochemical tests were conducted without further material optimization. The electrode active material load was approximately 3 mg/cm^2. Figure 1a shows the galvanostatic charge/discharge voltage profiles of the $Na_{0.78}Ni_{0.23}Mn_{0.69}O_2$ electrode during the first, second, third, fourth, fifth, 10th, and 20th cycles, at 0.1 C cycling rate. The material delivers a reversible first cycle capacity of 138 mAh g^{-1} when cycled between 2−4.5 V, with a low Coulombic efficiency of 75%. In subsequent cycles, the plateau above 4.1 V vanishes, and the Coulombic efficiency increases to 97%. The differential capacity ($dQ\ dV^{-1}$) versus voltage plots shown in Figure 1b clearly reveal that the long high voltage plateau is irreversible upon cycling. Of note, the 180 mAh g^{-1} first charge capacity (equivalent to the removal of 0.66 Na per formula unit) is significantly higher than the theoretical value of 121 mAh g^{-1} calculated on the basis of the Ni^{2+}/Ni^{4+} redox change. In addition, the long plateau between 4.1 and 4.5 V indicates a high voltage reaction pathway different from the one observed in the low voltage region (2.0−4.1 V). As shown in Figure S2, the behavior in the low voltage region remains unchanged over a large range of applied current densities (12−300 mA g^{-1}); on the other hand, the high voltage plateau shortens significantly at higher charging currents, indicating that this high voltage reaction is kinetically slow. Figure 1c shows the voltage profiles of the $Na_{0.78}Ni_{0.23}Mn_{0.69}O_2$ electrode discharged at different current rates, ranging from 0.1 to 5 C. The material still provides a high reversible capacity of 120 mAh g^{-1} at a 5 C discharge rate, corresponding to approximately 87% of the capacity observed when cycled at a lower rate of 0.1 C. This performance is among the best reported thus far for Na layered oxide materials.[24] Figure 1d shows the cycling performance of the $Na_{0.78}Ni_{0.23}Mn_{0.69}O_2$ cathode when charged and discharged at various current rates. A 0.1 C cycling (charge/discharge) rate was initially applied and progressively increased, as indicated in the figure. The discharge capacity is close to 125 mAh g^{-1} after 10 cycles. An increase in the current density from 0.2 to 0.5 C, and then to 1.0 C, results in negligible capacity decrease. Even after a 100-fold current density increase (10 C), the discharge capacity is still 75 mAh g^{-1}, which is 60% of the total capacity cycled at 0.1 C. After the current density was set back to 0.1 C, the material exhibits a capacity of 124 mAh g^{-1}, exceptionally close to the initial capacity. The high capacity retention discussed above attests to the resilience of the P2− $Na_{0.78}Ni_{0.23}Mn_{0.69}O_2$ material to harsh cycling conditions, and to fast Na-ion diffusion in the structure.

To investigate the origins of the first charge excess capacity further, electrochemical impedance spectroscopy (EIS) experiments were conducted on the P2−$Na_{0.78}Ni_{0.23}Mn_{0.69}O_2$ electrode using a three-electrode Swagelok T-cell. This configuration allows for proper impedance isolation of the working electrode, while eliminating the effects of the Na metal counter electrode.[38] The material was cycled to a specific state of charge (SOC) and allowed to reach equilibrium (2 h rest) before the acquisition of impedance data. After each impedance measurement, the cell was cycled to the next voltage step and the process was repeated. Figure S3(a) shows the Nyquist plots of the working electrode at 3.5, 4.1, and 4.5 V, and after a second charge to 4.5 V. Upon electrochemical cycling, the electrode experiences a series of processes in the bulk and at the surface, resulting in different suppressed semicircles in the Nyquist plots shown in Figure S3. An equivalent circuit is required to fit the data at different SOCs and deconvolute the impedance response into the various components of the electrochemical cell. The model accounts for the ohmic resistance of the electrolyte (R_Ω), the double layer capacitance of the electrode/electrolyte interface (CPE_f), the resistance due to irreversible side reactions (R_f), the charge transfer resistance (R_{ct}), and the solid-state diffusion impedance also known as the Warburg impedance (Z_w).[38−41] Electrochemical parameters associated with the equivalent circuit are summarized in Table S1. As expected, R_Ω does not change significantly upon electrochemical cycling. Below the plateau region (<3.5 V), the combined resistance of the two suppressed semicircles is 184.5 Ω. At 4.1 V, there is a slight increase in R_f due to electrolyte decomposition. Over the long voltage plateau, between 4.1 and 4.5 V, the charge transfer resistance increases significantly as a result of the formation of a solid electrolyte interphase (SEI) layer and properties of the particle surface (140.4−260 Ω, respectively). A similar increase was observed in a number of Li-excess cathode materials.[40,41] As mentioned earlier, the long high voltage plateau contributes to the excess capacity in the first cycle but does not persist in the following cycles (see Figure 1). The EIS spectra obtained on first and second charge are also very different: the total cell resistance upon second charge is significantly lower (165.7 Ω) than the resistance observed upon first charge (290.1 Ω), the latter resulting from irreversible surface reactions and structural reorganization during the initial charging process.

2.2. Structural Evolution of the $Na_{0.78}Ni_{0.23}Mn_{0.69}O_2$ Electrode upon Cycling. As reported in earlier work, Ni- and Mn-containing layered oxide cathode materials are prone to P2/O2 phase transformations upon charge above 4.2 V. The P2 phase is reversibly generated upon subsequent discharge to 2.5 V.[6,20] Although fast Na-ion diffusion can be achieved in the initial P2 phase, the high voltage phase transformation is detrimental to the electrochemical performance of the cathode and inevitably leads to poor rate and cycling capabilities. By limiting the cutoff voltage to 4.1 V, the cycling performance can be largely improved, yet at the expense of more than 40% of the total capacity.[20] The excellent electrochemical properties of the $Na_{0.78}Ni_{0.23}Mn_{0.69}O_2$ electrode suggest that the bulk structure stays P2 and exhibits good Na-ion diffusion properties upon removal of 0.66 Na per formula unit.

Structural changes in the $Na_xNi_{0.23}Mn_{0.69}O_2$ electrode during electrochemical cycling were monitored by analyzing samples stopped at different SOCs using ex situ synchrotron XRD. Lattice parameters were obtained from Rietveld refinements of the XRD patterns. As shown in Figure 2a, the XRD pattern of
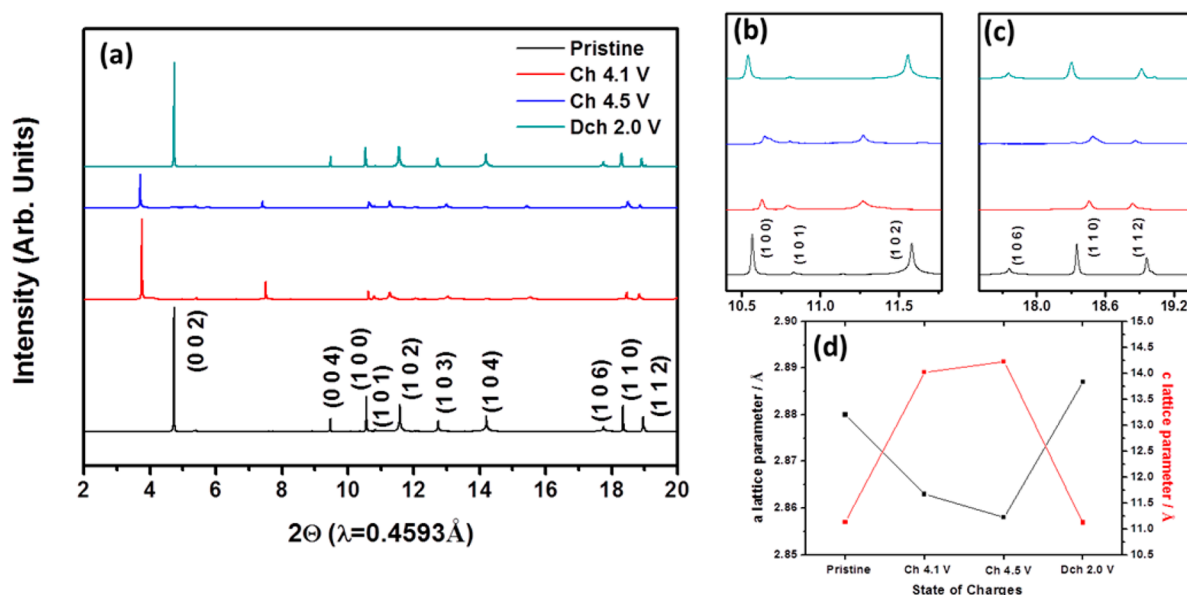
Figure 2. (a) Synchrotron X-ray diffraction patterns of $Na_{0.78}Ni_{0.23}Mn_{0.69}O_2$ electrodes stopped at different states of charge (SOCs) during the first electrochemical cycle, (b,c) enlarged regions of the XRD patterns containing the (100), (101), (102), (106), (110), and (112) peaks, and (d) evolution of the a and c lattice parameters during the first charging process, as determined from Rietveld refinements.
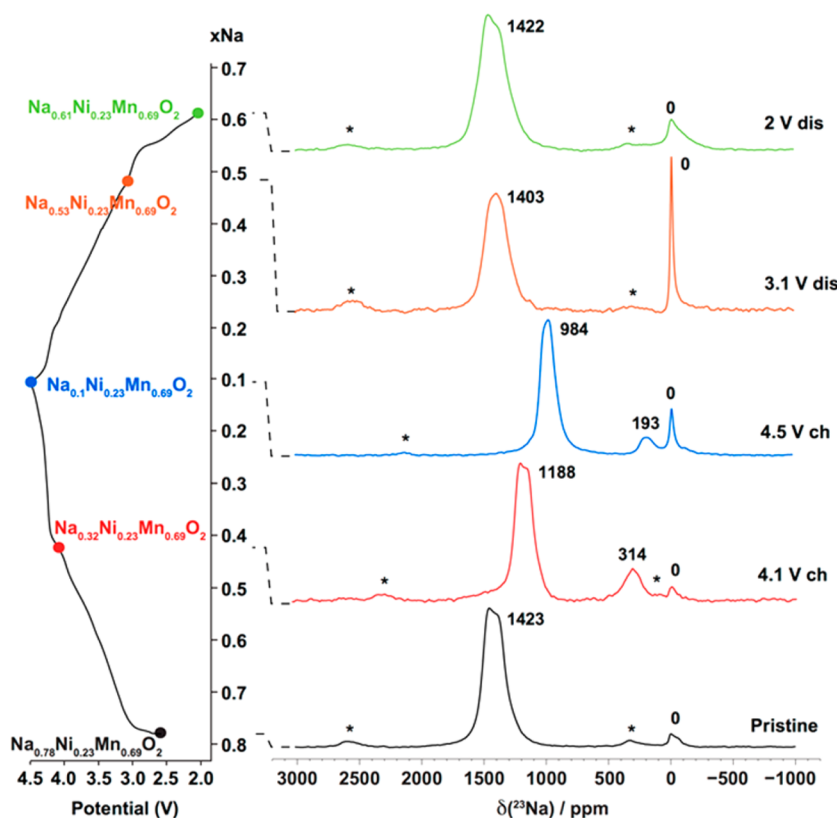

Figure 3. ^{23}Na NMR spectra acquired on as-synthesized P2−$Na_{0.78}Ni_{0.23}Mn_{0.69}O_2$ and on electrodes stopped at four different SOCs along the first electrochemical cycle. The spectra were collected at room temperature, 60 kHz MAS (magic angle spinning), and at an external field of 4.7 T. Spinning sidebands are denoted with "*". The diamagnetic signal at 0 ppm is presumably due to residual Na_2CO_3 starting material in the spectrum obtained on the as-prepared sample, and to electrolyte decomposition products formed upon cycling in the spectra collected upon charge and discharge.

the pristine sample is well indexed in the hexagonal space group $P6_3/mmc$, confirming that the as-synthesized material is P2-type and phase pure. Besides, as observed in similar layered materials,[23,44] a small concentration of stacking faults is

expected in this compound, causing unconventional peak profiles, which will be discussed in detail later. The XRD patterns of the partially charged (4.1 V) and fully charged (4.5 V) samples can also be fitted in the $P6_3/mmc$ space group
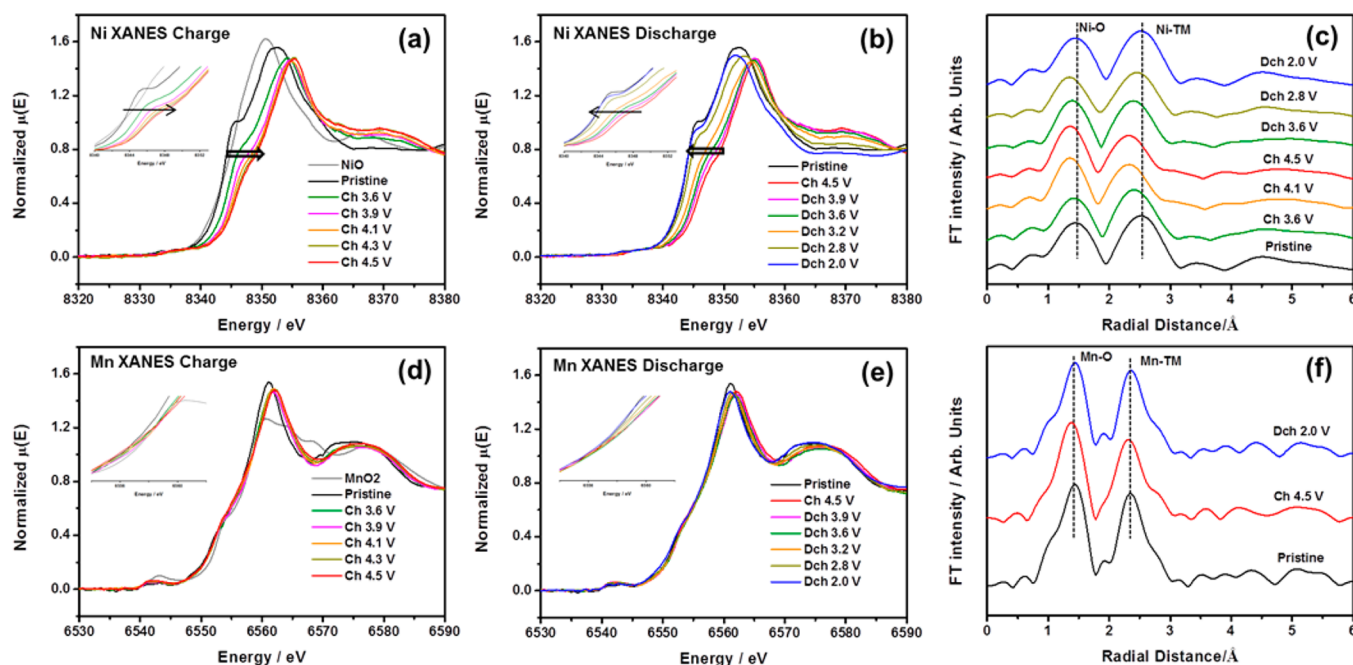
Figure 4. In situ XAS analysis of $Na_{0.78}Ni_{0.23}Mn_{0.69}O_2$ electrodes at different SOCs during the first electrochemical cycle: (a,b) XANES spectra at Ni K-edge, (d,e) XANES spectra at Mn K-edge, and (c,f) corresponding EXAFS spectra.

(Figure S4), demonstrating that the overall P2 crystal structure is maintained upon Na extraction. The *a* lattice parameter, dominated by the TM-TM distance, decreases upon charge, as expected from the increase in the average Ni oxidation state, resulting in a shift of the (100) peak to higher angles. On the other hand, the *c* lattice parameter increases significantly, as demonstrated by clear shifts of the (002) and (004) peaks (see Figure 2a), and of the (10*l*) and (11*l*) peaks (see Figure 2b and c), to lower angles. The screening effect of Na ions in the interlayer space becomes less effective, and Coulombic repulsion between successive O layers increases upon Na deintercalation. However, electrostatic effects are not sufficient to account for the drastic increase in *c* lattice parameter upon charge, from 11.128 to 14.224 Å. Previous studies on Na_xTMO_2 cathodes have speculated that solvent molecules, as well as salt ions, can insert between the TMO_2 layers upon Na removal.[17,42-44] The interlayer distance at 4.5 V charge, around 7 Å, is close to the values obtained for the high voltage phases in these previous reports, suggesting that Na-ion removal from $P2-Na_{0.78}Ni_{0.23}Mn_{0.69}O_2$ leaves the crystal structure vulnerable to the insertion of solvent molecules. Lower XRD peak intensities are observed upon Na deintercalation, especially for the fully charged (4.5 V) sample. Moreover, the patterns shown in Figure 2b and c reveal a broadening of the XRD peaks at high voltage, which may indicate that O2 stacking faults are formed in the electrode material.[23] The XRD pattern and lattice parameters obtained for the fully discharged sample are very similar to those obtained for the pristine material, indicating good structural reversibility upon Na reinsertion. On the basis of these observations, it is speculated that the larger Na content of *x* = 0.78 in the as-synthesized material, as compared to conventional P2-type materials with a Na content of *x* = 2/3, prevents oxygen layer shifts and stabilizes the P2 framework, leading to the excellent performance shown in Figure 1.

While XRD probes long-range structural order, NMR gives insight into local structural changes in the material upon

cycling. ^{23}Na NMR spectra were acquired on as-synthesized $Na_{0.78}Ni_{0.23}Mn_{0.69}O_2$ and at different SOCs during the first cycle (Figure 3). The major resonance at ca. 1400 ppm in the pristine spectrum is an average signal resulting from fast Na-ion motion (on the NMR time scale) between edge and face sharing prismatic sites in the structure, as reported in our recent NMR study on related $P2-Na_x[Li_yNi_zMn_{1-y-z}]O_2$ ($0 \leq x, y, z \leq 1$) materials.[44] This average Na resonant frequency gradually decreases to ca. 1200 ppm at 4.1 V SOC, and to ca. 1000 ppm at 4.5 V SOC, as expected from Ni oxidation, and the reduction of the number of unpaired electrons centered on the nickel ions (from two for Ni^{2+} to none for Ni^{4+}).[44] An additional NMR peak is present at ca. 300 ppm at 4.1 V, and at ca. 200 ppm at 4.5 V. These Na signals are attributed to Na environments created upon water intercalation into the Na deficient layers, on the basis of prior work on related materials.[44] The low resonant frequencies result from the expanded layers, longer TM−O− Na bonds, and weaker TM−Na interactions.[44] The integrated area under the low frequency peaks reveals that Na ions in hydrated layers represent less than 1/10th of all 0.1 Na left in the material at 4.5 V; this is a much lower proportion than what was previously observed in similar materials,[44] suggesting little water uptake in the ex situ (charged) samples. The NMR signal assigned to the average prismatic Na environment remains highest in intensity throughout cycling, which testifies to a highly stable P2 structure upon Na extraction and is consistent with XRD results. The major peak shifts back to ca. 1400 ppm in the fully discharged state, clearly demonstrating the reversibility of the P2 structure upon Na extraction and reinsertion. Overall, XRD and ^{23}Na NMR results demonstrate that the long-range P2 structure of the $Na_{0.78}Ni_{0.23}Mn_{0.69}O_2$ cathode material is stable and that local structural order is recovered upon cycling. As calculated from the first charge capacity, the amount of Na left in the structure at 4.5 V is around 0.12 Na per formula unit. The residual Na ions are critical to maintain structural stability. The changes observed in the long- and short-range structure upon electrochemical
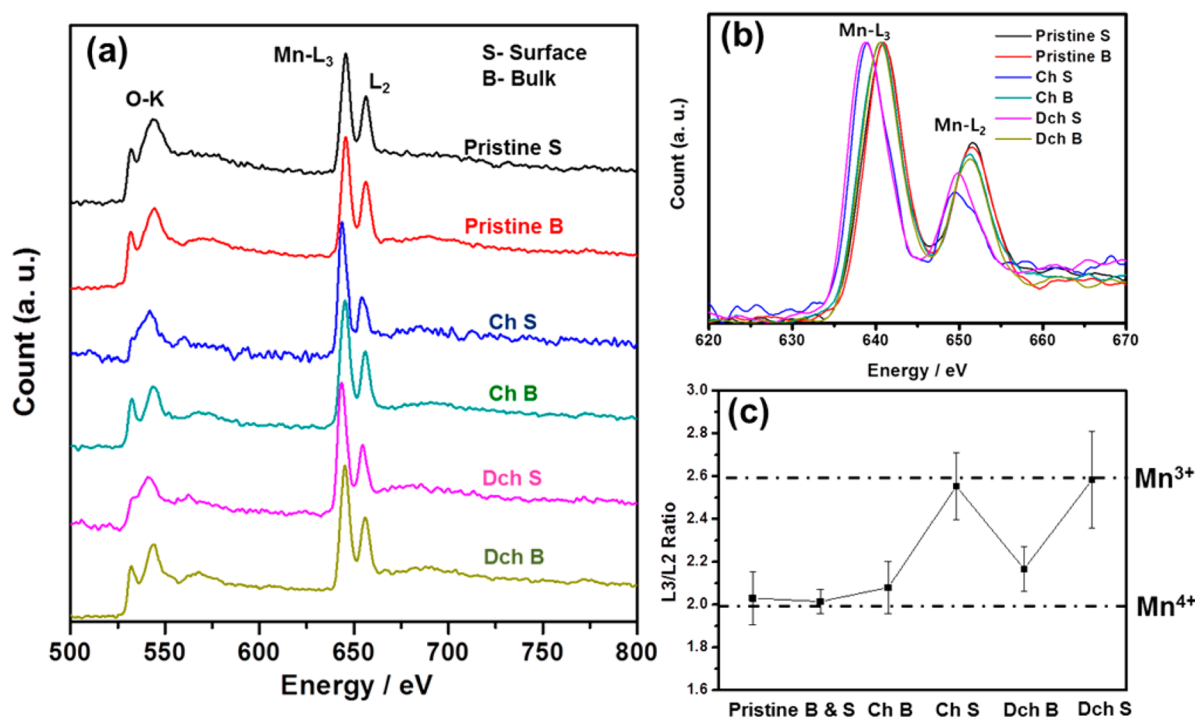
Figure 5. EELS spectra of the (a) O K-edge and (a and b) Mn L-edge measured at the surface (S) and in the bulk (B) of pristine and electrochemically cycled $Na_xNi_{0.23}Mn_{0.69}O_2$ particles. (c) The corresponding Mn L_3/L_2 ratio.

cycling do not account for the large excess capacity observed during the first charge. Therefore, redox reactions taking place in the material were examined in more detail using in situ XAS.

2.3. Bulk Electronic Structure Study Using In Situ XAS. The evolution of the electronic structure and variations in the nickel and manganese local environments during the first cycle were investigated with in situ X-ray absorption spectroscopy (XAS) (Ni, 8333 eV; Mn, 6539 eV). In particular, time-resolved information on the Ni valence state is crucial to unveil the redox reaction mechanisms taking place upon electrochemically cycling the material. Comparing the standard references, NiO and MnO_2, to XAS data obtained for as-synthesized $Na_{0.78}Ni_{0.23}Mn_{0.69}O_2$, it is evident that the pristine material predominantly consists of Ni^{2+} and Mn^{4+} ions (Figure 4a and d). The Ni K-edge shifts to a higher energy region upon charge, indicating that Ni^{2+} is oxidized. The energy shift at 4.5 V is ~4 eV, which is much larger than the shift expected for the Ni^{2+}/Ni^{3+} redox change (~2 eV, Figure S5), suggesting that the oxidation state of Ni is close to Ni^{4+}.[44,45] The inset of Figure 4a reveals that most of the energy shift of the Ni K-edge takes place below 4.1 V, while a minor energy shift is observed between 4.1 and 4.5 V. These results indicate that, to a large extent, the Ni charge transfer reaction takes place in the lower voltage region. Upon subsequent discharge to 2.0 V, Ni ions are reduced back to their divalent state, demonstrating that the Ni redox reaction is completely reversible.

Ni EXAFS results are shown in Figure 4c, where the two shells at 1.4 and 2.6 Å represent the Ni−O interaction and Ni−TM interaction, respectively. As Ni^{2+} is oxidized to Ni^{4+}, both the Ni−O and the Ni−TM interatomic distances decrease. These changes account for the *a* lattice parameter decrease observed in the XRD patterns upon charge. The variations in Ni−O and Ni−TM bond lengths are fully reversible upon subsequent discharge, and the interatomic distances ultimately return to their original values.

In contrast, Mn ions show only a minor participation in the electrochemical charge transfer reaction and remain essentially all Mn^{4+} (Figure 4d and e). Figure 4f reveals a slight change in the Mn−TM bond distance at the fully charged state, presumably resulting from the shorter bond lengths around the Ni^{4+} ions. Trace amounts of Mn^{3+} are present in the fully discharged sample, as evidenced by the slight shift of the Mn K-edge toward lower energies, as compared to the pristine state. This phenomenon will be discussed in a later section. Overall, it is clear that tetravalent Mn ions are electrochemically inactive and their main function is to stabilize the layered structure. On the other hand, Ni^{2+}/Ni^{4+} is the major redox active couple. Given that most of the Ni^{2+}/Ni^{4+} redox occurs below 4.1 V on charge, a different charge transfer mechanism must contribute to the capacity in the high voltage plateau region, between 4.1 and 4.5 V. The tetravalent Mn-ions are inactive, giving rise to the hypothesis that the lattice oxygen participates in the high voltage charge compensation process; these observations are similar to those previously observed in lithium-excess cathode materials for LIB systems,[25,46] where considerable work has been performed to test this hypothesis. To explore this further, the EELS and soft XAS techniques are used here to investigate the electronic structure of the TM−O ligand in the material.

2.4. Surface and Bulk Characterization by EELS and Soft XAS. STEM coupled with EELS was employed to study the evolution of the surface structure of electrochemically cycled $Na_xNi_{0.23}Mn_{0.69}O_2$ particles. Electron microscopy data obtained on the as-synthesized material and on samples after initial charge are shown in Figure S6. The layered structure of the P2 material is clearly observed along the [010] zone axis of the pristine particle (Figure S6(a)). The bright dots indicate the lighter element (here Na), while the dark dots represent the heavier TM ions. Stacking faults and defects, indicated with red circles, are also observed in the pristine material. The presence of structural defects makes it difficult to acquire high-resolution
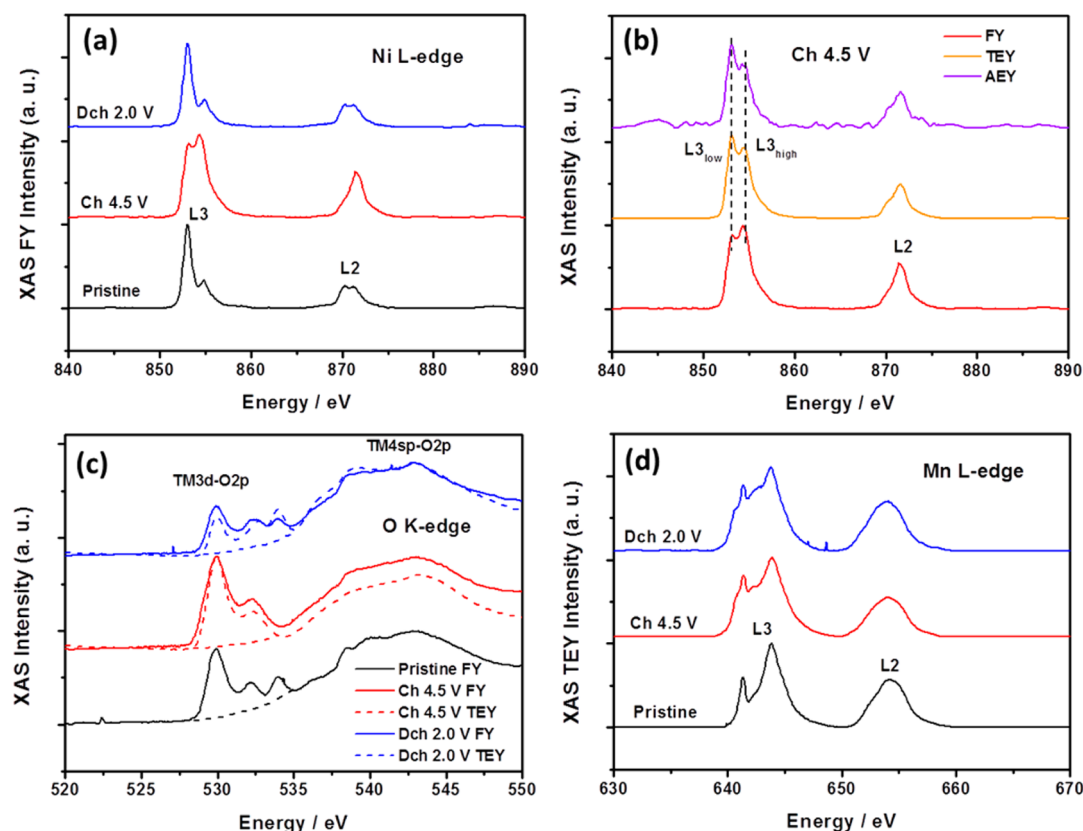
Figure 6. (a) Ni L-edge XAS spectra of electrochemically cycled $Na_{0.78}Ni_{0.23}Mn_{0.69}O_2$ electrodes in FY mode, (b) Ni XAS L-edge spectra of the fully charged electrode using AEY (purple), TEY (yellow), and FY (red) modes, (c) O K-edge XAS spectra in FY and TEY modes, and (d) Mn L-edge XAS spectra of electrodes cycled to different SOCs using TEY mode.

STEM images, because atoms are not perfectly aligned along a single direction (Figure S6(c)). The HRTEM image shown in Figure S6(b) was obtained on a cycled particle along the [001] zone axis. An amorphous SEI layer around 3−5 nm thick is observed at the surface of the particles. A large number of defects are also present in the bulk of the cycled particles, resulting in blurry high-resolution STEM images.

Figure 5a and b compares the EELS spectra obtained at the O K-edge and at the Mn L-edge for pristine and cycled particles. The evolution of the fine structure and energy position of the O−K and Mn−L edges give insight into electronic structure changes taking place in the material upon cycling. The Mn L-edge energy positions and fine structures are nearly identical at the surface and in the bulk of pristine particles, as well as in the bulk of cycled particles. At the surface of cycled particles, however, the Mn-L edge moves to a slightly lower energy, suggesting a decrease in the average Mn oxidation state. In addition, the higher L3/L2 ratio, indicative of the TM oxidation state, is further evidence for a lower Mn oxidation state at the particles' surface.[47] Differences in the O K-edge fine structure are observed between the spectra obtained at the surface of cycled particles and those collected on pristine particles. The first peak at an energy loss of 532 eV (indicated with a dashed line) almost vanishes in the spectra obtained at the surface of cycled particles. This oxygen prepeak can be attributed to the electronic transition from the 1s core state to the O 2p−TM 3d hybridized states. The decrease in intensity of this peak at the surface of cycled particles indicates fewer holes in the 2p−3d hybridized orbitals, meaning that surface TMs are in a lower valence state. Moreover, EELS

spectra obtained from a single particle at different surface depths (from surface to bulk) reveal a gradient of TM valence states, as depicted in Figure S7.

Similar distributions of TM oxidation states across particles, oxygen vacancies formed at or near the surface of the particles, and variations between bulk and surface electronic structures have been extensively reported in Li-excess LIB cathodes.[41,48,49] Different models have been proposed to describe the electronic and structural phenomena upon charge, such as the transition state theory model and the metal densification model.[48,50] Although the exact reaction mechanisms are still under debate, it has been widely recognized that these transitions are associated with lattice oxygen evolution occurring at high voltage charge compensation. Here, the similar electronic structure changes observed on the cycled $Na_xNi_{0.23}Mn_{0.69}O_2$ particles, as in Li-excess cathodes, strongly suggest that lattice oxygen in the P2 material participates in the charge compensation mechanism at high voltage. While the details of interactions between TMs and oxygen vacancy are still unclear for Na P2-type structures, the present study proves that oxygen-based redox processes can contribute to the observed capacity in NIB layered oxide cathodes. The ensemble-averaged sXAS technique is employed to confirm this statistically.

Soft XAS (sXAS) is capable of probing chemical environments with excellent surface depth sensitivities by tuning the signal acquisition mode. Specifically, sXAS data can be collected simultaneously using three detection modes: (1) Auger electron yield (AEY), (2) total electron yield (TEY), and (3) fluorescence yield (FY). Electron yield modes vary in penetration depth and are extremely surface sensitive: TEY

mode has a probing depth of 2−5 nm, while AEY has a probing depth of 1−2 nm. The FY mode probes the bulk of the material up to a depth of about 50 nm.[51] Given its impressive capabilities, this characterization technique has been applied to investigate charge compensation mechanisms in LIB cathode materials, proving particularly useful in the exploration of redox reaction mechanisms involving oxygen anions in relation to those involving TM ions.[51,52] Here, it was used to further test the hypothesis of oxygen activity in our NIB cathode material.

X-ray absorption peaks corresponding to the metal L3- and L2-edges are relatively intense because the 2p−3d transition is electric dipole-allowed. In addition, these peaks are very sensitive to oxidation state, spin state, and bond covalence. The most salient electronic structure can be qualitatively obtained by deconvoluting the L3-edge into high-energy ($L3_{high}$) and low-energy ($L3_{low}$) features. Of note, the ratio between the $L3_{high}$ and $L3_{low}$ integrated peak intensities is in a positive relationship with the TM oxidation state.[53]

The Ni L-edge spectra obtained in FY mode for the ex situ samples collected during the first cycle are shown in Figure 6a. The pristine spectrum clearly demonstrates that Ni is in its divalent state, the split L3-edge feature being consistent with previous reports.[11,54,55] The bulk Ni oxidation state increases and decreases upon charge and discharge, respectively, in good agreement with the in situ XAS data discussed earlier. The average Ni oxidation is close to Ni^{4+} at the end of charge, although a slight self-discharge might happen given the high voltage of the ex situ cell.[56] Ni L-edge data collected on the fully charged electrode using the three different detection modes are compared in Figure 6b. A clear decrease in the nickel oxidation state is observed from the bulk to the surface of the charged $Na_xNi_{0.23}Mn_{0.69}O_2$ particles, as evidenced by the gradual decrease in the $L3_{high}$ to $L3_{low}$ ratio when going from FY to TEY, to AEY mode.[55] As discussed earlier, a number of reports on lithium-excess cathode materials have shown that surface structural changes and TM redistribution give rise to TM oxidation state gradients within the particles.[51,57,58]

Pre-edge peak positions and intensities in the ligand K-edge XAS spectra provide important structural information on the chemical bonding between ligand and metal atomic species. The O K-edge XAS of electrochemically cycled $Na_xNi_{0.23}Mn_{0.69}O_2$ is shown in Figure 6c. The pristine O K-edge XAS spectra can be divided into two regions. Pre-edge peaks below 535 eV are attributed to electronic transitions from the O 1s state to the O 2p−TM 3d hybridized state. On the other hand, the broad peaks above 535 eV correspond to transitions to O 2p−TM 4sp hybridized states.[59] In general, the 2p−3d hybridized band can be further divided into a lower energy peak around 529.8 eV, corresponding to the t_{2g} band, and a higher energy peak around 532.2 eV, corresponding to the e_g band. The peak around 534.0 eV is associated with some sodium oxides or carbonaceous components that exist on the surface of the active material particles.[60] Because the density of the empty bound state in the molecular energy level is related to the hybridization of the O 2p−TM 3d orbitals, the integrated pre-edge peak intensity gives key information on the average hole state distribution and the average effective charge on oxygen anions.[52,58] The increase in the prepeak intensity observed upon charge is consistent with Ni L-edge FY results: Ni oxidation creates more holes in the 2p−3d hybrid orbitals, resulting in an increase in the O prepeak in FY mode. On the other hand, the smaller prepeak in the O TEY spectra demonstrates that 2p−3d orbitals on the particles' surface have

more electrons, especially in the antibonding e_g orbital. This is a clear indication that TM ions are in a lower valence state at the surface, in agreement with the Ni TEY and AEY results.

As observed in Li-excess cathode materials, TM oxidation state gradients associated with lattice oxygen charge compensation processes are expected to take place concurrently with structural and electronic phenomena at the surface of the particles.[41,48] For the fully discharged sample, the intensity of the O prepeak is lower in TEY mode than in FY mode, presumably due to irreversible structural changes at the surface of electrode particles during the charging process. Although O K-edge spectra were also acquired in AEY mode, the peaks assigned to the active material were largely masked by peaks from O-containing residual electrolyte and SEI components. Mn L-edge TEY results are shown in Figure 6d. A slight decrease in the Mn oxidation state is observed upon cycling. In fact, the Mn L-edge spectra collected on charge and discharge are similar to those obtained for Mn in Li spinel structures, where Mn was shown to be reduced at the surface.[58]

Overall, the sXAS results presented in this section complement the EELS results presented earlier. The bulk to surface TM valence state gradient observed for electrochemically cycled particles suggests that lattice oxygen redox processes take place upon charge. In addition, sXAS data provide clear evidence for electronic and structural changes at the surface of the particles. The excess capacity and high surface resistance observed during the initial charge process presumably result from a reaction mechanism comparable to that reported for Li-excess LIB cathodes.

2.5. Exploring Oxygen Activity in a Na Cathode Material.
In Li-excess oxide cathode materials, the participation of oxygen anions in the charge compensation mechanisms upon electrochemical cycling results in a remarkably high capacity, and this family of compounds is currently under intense scrutiny for the development of next generation Li batteries.[25] The similar physicochemical properties of Na and Li have encouraged us to design a Na layered TM oxide that displays oxygen anion redox activity comparable to that observed for Li-excess LIB cathodes. In this study, we showed that the $Na_{0.78}Ni_{0.23}Mn_{0.69}O_2$ cathode delivers a first charge capacity of 180 mAh g^{-1} and discharge capacity of 138 mAh g^{-1}, which are both higher than the theoretical capacity of 121 mAh g^{-1}. The charge compensation mechanism was carefully studied using a number of advanced characterization techniques. As shown in Figure 7, the Ni^{2+} to Ni^{4+} redox couple is active over the potential slope region, extending from the open current potential (OCV) to 4.1 V during the first charge, while oxygen anions are involved in the charge compensation mechanism over the high voltage plateau. The plateau region accounts for 60 mAh g^{-1} of excess capacity on first charge. The lattice oxygen reaction is concurrent with the formation of a surface to bulk TM oxidation state gradient, as well as with structural transformations at the surface of the cycled particles. Yet the high voltage oxygen redox processes in this material are not as reversible as in Li-excess compounds; the present work clearly proves that oxygen charge compensation can take place in P2-type Na cathodes.

It is speculated that the particular Na to TM ratio in the cathode material of interest to the present study is the cause for oxygen reactions. The stoichiometry of the compound, $Na_{0.75}Ni_{0.24}Mn_{0.69}O_{1.99}$ (normalized to Mn), was determined by ICP-OES and confirmed by Ni/Mn K-edge XAS. In addition, ^{23}Na NMR indicated that all Na ions are located in
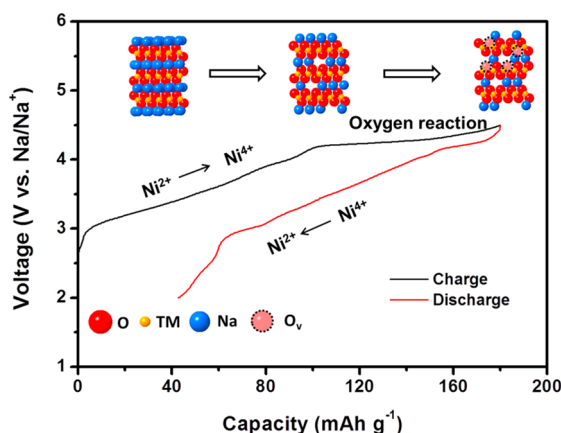
Figure 7. Charge compensation mechanisms in the P2−$Na_{0.78}Ni_{0.23}Mn_{0.69}O_2$ cathode.

the prismatic layers. Therefore, seven percent of vacancies per formula unit are expected in the transition metal layer, introducing defects in the pristine material. As shown in Figure S8(a,b), the ($10l$) XRD peaks are much broader than the ($h00$) and ($00l$) peaks, the latter two being normal and parallel to the metal planes, respectively, suggesting the existence of through-plane stacking faults in the pristine material;[61] this is also supported by HRTEM data in Figure S6(a). The effect of TM vacancies is reflected by the Ni/Mn K-edge EXAFS (Figure S8(c,d)). As compared to a previous sample ($Na_{0.8}Li_{0.12}Ni_{0.22}Mn_{0.66}O_2$), in which the TM sites are fully occupied,[23] the relative intensity of the peak resulting from the TM−TM interaction is slightly smaller for the current compound, indicating fewer TM ions in the first cation coordination shell surrounding both Ni and Mn. Fitting of EXAFS spectra is complicated by the presence of these through-plane stacking faults in the pristine $Na_{0.75}Ni_{0.24}Mn_{0.69}O_{1.99}$ material, resulting in large σ^2 and E_0 values (Table S2).

Previous work by Dahn et al. on a lithium layered oxide containing TM vacancies showed that high irreversible capacity was associated with oxygen release. At the time, no clear mechanism was proposed to explain this phenomenon. Two more recent studies by Bruce et al.[29] and Ceder et al.[30] provided insights into the potential mechanisms leading to O participation in the redox processes, which may also apply to the present study. In Li-excess materials, part of the Li^+ removed upon charge can be compensated by the formation of localized electron holes on the O atoms. The requirement for O redox is to have an essentially unhybridized 2p orbital on O, which is only possible in the case of highly ionic bonding (e.g., in Li−O−Li configurations). Extending the above argument to compounds featuring vacancies in the TM layer, either a Li−O−vacancy or a Na−O−vacancy configuration can potentially also fulfill this requirement. We tentatively suggest that electrons from O atoms in these ionic environments can participate in the charge compensation during delithiation/desodiation and contribute to the excess capacity observed during the charge process. As noted, the localized electron holes on oxygen render the oxygen unstable and susceptible to elimination from the lattice. Whether oxygen loss or oxygen redox chemistry dominates relies on the stability of the oxidized lattice O atoms in the crystal structure. In this particular P2 structure, due to the larger interlayer repulsion of AA stacking, it is likely that oxygen vacancies form in the high voltage

plateau region, causing irreversible capacity during the first cycle. Work is ongoing to understand the detailed oxygen reaction mechanism in layered TM oxide NIB cathodes and to identify new material design principles to improve the reversibility of the oxygen-based redox processes (e.g., different TMs, different oxygen stacking); the results will be discussed in a future publication.

3. CONCLUSION

In summary, a new $Na_{0.78}Ni_{0.23}Mn_{0.69}O_2$ cathode shows outstanding electrochemical performance for rechargeable sodium-ion battery applications. The P2 structure of this material is stabilized over a wide voltage window, from 2.0 to 4.5 V. The stable framework facilitates Na intercalation/deintercalation during the electrochemical cycling process and ensures excellent rate performance. The electrochemical reaction is mainly based on the Ni^{2+}/Ni^{4+} redox couple, while Mn is electrochemically inactive and is stabilized as Mn^{4+} in the bulk of the material. An irreversible reaction taking place upon initial charge and resulting in capacity degradation in the first cycle was carefully studied. It is found that the excess capacity during the first charge mainly comes from the high voltage region and is strongly affected by kinetic factors. EELS and sXAS results indicate a gradient distribution of TM oxidation states from the surface to the bulk of the electrochemically cycled particles. This gradient is closely related to the formation of oxygen vacancies at the surface of material. Therefore, it is proposed that oxygen anions are involved in the charge compensation process upon initial charge, leading to an additional plateau at high voltage. This is the first time that compelling evidence is provided for oxygen vacancies in Na-ion layered oxide materials. We believe that the Na to TM ratio has a strong influence on the behavior and structural stability of layered oxide materials. Further work is required to improve the reversibility of oxygen-based redox processes on extended cycling.

4. EXPERIMENTAL SECTION

4.1. Material Synthesis and Characterization. An appropriate amount of Na_2CO_3 (molar ratio of carbonate ions to transition metal ions is 1:1) was dissolved in 60 mL of deionized water, then added dropwise to a 10 mL mixed solution of $Ni(NO_3)_2$ and $Mn(NO_3)_2$ (Ni:Mn = 1:3 in molar ratio) while stirring. The solution then was transferred to a 100 mL Teflon-lined stainless steel autoclave and aged at 80 °C for 12 h, yielding $(Ni_{0.25}Mn_{0.75})CO_3$. The $(Ni_{0.25}Mn_{0.75})CO_3$ particles were mixed with a stoichiometric amount of Na_2CO_3, and the mixture was calcined at 900 °C for 12 h in a 50 mL porcelain crucible. The stoichiometry of the as-synthesized compound was determined by inductively coupled plasma-optical emission spectroscopy (ICP-OES), and the formula of $Na_{0.75}Ni_{0.24}Mn_{0.69}O_{1.99}$ (normalized to Mn) was confirmed. The morphology of the as-synthesized material was characterized by a Philips XL30 environmental scanning electron microscope (ESEM) operating at 10 kV.

4.2. Synchrotron X-ray Diffraction (XRD). The samples characterized by XRD were obtained by disassembling the cycled batteries in an argon-filled glovebox. The electrode materials were washed using battery grade dimethyl carbonate (DMC) three times, then stripped off from the aluminum current collectors. The powders from the cycled electrodes were then mounted in hermetically sealed capillary tubes for ex situ XRD measurements. Synchrotron powder diffraction patterns of all samples were collected at the Advanced Photon Source (APS) on beamline 11-BM (λ = 0.459 Å). The beamline uses a sagittal focused X-ray beam with a high precision diffractometer circle and 12 independent analyzer sets, providing high

sensitivity and resolution. XRD patterns were collected between $-6.5°$ and $28.0°$ in 2θ angles.

4.3. Nuclear Magnetic Resonance (NMR). ^{23}Na ssNMR spectra were acquired at room temperature on a Bruker Avance III 200 wide-bore spectrometer (4.7 T external magnetic field) at a Larmor frequency of -53.0 MHz. All NMR experiments were performed under 60 kHz magic angle spinning (MAS) using a 1.3 mm double-resonance HX probe and a recycle delay of 30 ms. ^{23}Na NMR chemical shifts were referenced against solid $^{23}NaCl$ at 7.21 ppm. ^{23}Na spin echo NMR spectra were acquired using a 90° radiofrequency (RF) pulse of 1.03 μs and a 180° RF pulse of 2.06 μs at 25.04 W. Transverse (T_2') relaxation times were determined from an exponential fit of the decay of the signal intensity obtained as the echo delay was increased in an NMR spin echo pulse sequence. The NMR data were processed with a 1 kHz applied line broadening.

4.4. In Situ X-ray Absorption Spectroscopy (In Situ XAS). X-ray absorption spectroscopy measurements were performed on the 5-BM-D beamline at the Applied Photon Source (APS) at Argonne National Laboratory. Customized coin cells were used to prevent sample contamination. Measurements were performed at the Ni and Mn K-edge under transmission mode using a gas ionization chamber to monitor the incident and transmitted X-ray intensities. A third ionization chamber was used in conjunction with Ni and Mn foil standards to provide internal calibration for the alignment of the edge positions. The incident beam was monochromatized using a Si (111) double-crystal fixed exit monochromator. Harmonic rejection was achieved using a rhodium-coated mirror. Each spectrum was normalized using the data processing software package IFEFFIT.

4.5. Soft X-ray Absorption Spectroscopy (sXAS). Soft XAS measurements were carried out on beamline 8-2 at the Stanford Synchrotron Radiation Laboratory. These measurements were conducted on powder samples pressed on Au foil to avoid contamination from the adhesive of the carbon tape. Data were acquired under ultrahigh vacuum (10^{-9} Torr) in a single load at room temperature in total electron yield (TEY) mode via the drain current method, in Auger electron yield (AEY) mode using a cylindrical mirror analyzer, and in fluorescence yield (FY) mode using silicon photodiodes.

4.6. Scanning Transmission Electron Microscopy/Electron Energy Loss Spectroscopy (STEM/EELS). Electron microscopy work was carried out on a Cs-corrected FEI Titan 80/300 kV TEM/STEM microscope equipped with a Gatan Image Filter Quantum-865. All STEM images and EELS spectra were acquired at 300 kV and with a beam size of ~0.7 Å. EELS spectra shown in this work were acquired from a square area of $\sim0.5*0.5$ nm with an acquisition time of 3 s and a collection angle of 35 mrad. HAADF images were obtained with a convergence angle of 30 mrad and a large inner collection angle of 65 mrad. To minimize possible electron beam irradiation effects, EELS and HAADF figures presented in this work were acquired from areas without prebeam irradiation. Mn L3 to L2 intensity ratio analysis was performed using the method described by Wang et al.[47]

4.7. Electrochemical Tests. Cathode electrodes were prepared by mixing 80 wt % active material with 10 wt % acetylene black and 10 wt % polyvinylidene fluoride (PVdF). A glass fiber GF/F (Whatman) filter was used as the separator, and 1 M $NaPF_6$ in propylene carbonate (PC) was used as the electrolyte. Battery assembly was carried out in an MBraun glovebox (H_2O < 0.1 ppm). Galvanostatic discharge and charge at various current densities were performed on an Arbin BT2000 battery cycler. Additionally, electrochemical impedance spectroscopy (EIS) measurements were carried out with AC frequencies ranging from 0.01 to 1×10^6 Hz on galvanostatically cycled electrodes stopped at various states of charge (open current voltage (OCV), 3.5, 4.1, and 4.5 V) and discharge (3.5, 2.0 V). The electrodes were assembled in a three-electrode Swagelok cell, where the active material was the working electrode, and Na metal served as the counter and reference electrode. The three-electrode cells were then cycled as described earlier. The three-electrode configuration allows for proper isolation of the working electrode impedance. A Solatron 1287 potentiostat was used to measure the impedance at different states of charge and discharge. An equivalent circuit model was fitted to the data to separate the impedance contributions from the various components of the cell using the Z view software (v. 3.4a, Scribner Associates, Inc.).

■ ASSOCIATED CONTENT

⑤ Supporting Information

The Supporting Information is available free of charge on the ACS Publications website at DOI: 10.1021/jacs.7b00164.

SEM for $Na_{0.78}Ni_{0.23}Mn_{0.69}O_2$; voltage profiles, EIS of the material; XRD refinement of charged materials; Ni K-edge XANES spectra; HRTEM, STEM/EELS information about pristine and cycled materials; and EXAFS fitting of $Na_{0.78}Ni_{0.23}Mn_{0.69}O_2$ and $Na_{0.8}Li_{0.12}Ni_{0.22}Mn_{0.66}O_2$ (PDF)

■ AUTHOR INFORMATION

Corresponding Authors
*cpg27@cam.ac.uk
*shirleymeng@ucsd.edu

ORCID 🄾
Wei Tong: 0000-0002-2878-1297
Ying Shirley Meng: 0000-0001-8936-8845

Notes
The authors declare no competing financial interest.

■ REFERENCES

(1) Armand, M.; Tarascon, J.-M. *Nature* **2008**, *451* (7179), 652.
(2) Han, M. H.; Gonzalo, E.; Singh, G.; Rojo, T. *Energy Environ. Sci.* **2015**, *8* (1), 81.
(3) Maazaz, A.; Delmas, C.; Hagenmuller, P. *J. Inclusion Phenom.* **1983**, *1* (1), 45.

(4) Komaba, S.; Takei, C.; Nakayama, T.; Ogata, A.; Yabuuchi, N. *Electrochem. Commun.* **2010**, *12* (3), 355.

(5) Miyazaki, S.; Kikkawa, S.; Koizumi, M. *Synth. Met.* **1983**, *6* (C), 211.

(6) Lu, Z.; Dahn, J. R. *J. Electrochem. Soc.* **2001**, *148* (11), A1225.

(7) Kundu, D.; Talaie, E.; Duffort, V.; Nazar, L. F. *Angew. Chem., Int. Ed.* **2015**, *54* (11), 3431.

(8) Hamani, D.; Ati, M.; Tarascon, J. M.; Rozier, P. *Electrochem. Commun.* **2011**, *13* (9), 938.

(9) Parant, J. P.; Olazcuaga, R.; Devalette, M.; Fouassier, C.; Hagenmuller, P. *J. Solid State Chem.* **1971**, *3* (1), 1.

(10) Molenda, J.; Stokłosa, A. *Solid State Ionics* **1990**, *38* (1−2), 1.

(11) Kataoka, R.; Mukai, T.; Yoshizawa, A.; Sakai, T. *J. Electrochem. Soc.* **2013**, *160* (6), A933.

(12) Yuan, D.; Hu, X.; Qian, J.; Pei, F.; Wu, F.; Mao, R.; Ai, X.; Yang, H.; Cao, Y. *Electrochim. Acta* **2014**, *116*, 300.

(13) Sathiya, M.; Hemalatha, K.; Ramesha, K.; Tarascon, J.-M.; Prakash, A. S. *Chem. Mater.* **2012**, *24*, 1846−1853.

(14) Billaud, J.; Clément, R. J.; Armstrong, A. R.; Canales-Vázquez, J.; Rozier, P.; Grey, C. P.; Bruce, P. G. *J. Am. Chem. Soc.* **2014**, *136* (49), 17243.

(15) Takeda, Y.; Akagi, J.; Edagawa, A.; Inagaki, M.; Naka, S. *Mater. Res. Bull.* **1980**, *15* (8), 1167.

(16) Delmas, C.; Fouassier, C.; Hagenmuller, P. *Physica B+C* **1980**, *99* (1−4), 81.

(17) Komaba, S.; Yabuuchi, N.; Nakayama, T.; Ogata, A.; Ishikawa, T.; Nakai, I. *Inorg. Chem.* **2012**, *51* (11), 6211.

(18) Kubota, K.; Yabuuchi, N.; Yoshida, H.; Dahbi, M.; Komaba, S. *MRS Bull.* **2014**, *39* (5), 416.

(19) Yabuuchi, N.; Komaba, S. *Sci. Technol. Adv. Mater.* **2014**, *15* (4), 43501.

(20) Lee, D. H.; Xu, J.; Meng, Y. S. *Phys. Chem. Chem. Phys.* **2013**, *15* (9), 3304.

(21) Talaie, E.; Duffort, V.; Smith, H. L.; Fultz, B.; Nazar, L. F. *Energy Environ. Sci.* **2015**, *8* (8), 2512.

(22) Kim, D.; Kang, S. H.; Slater, M.; Rood, S.; Vaughey, J. T.; Karan, N.; Balasubramanian, M.; Johnson, C. S. *Adv. Energy Mater.* **2011**, *1* (3), 333.

(23) Xu, J.; Lee, D. H.; Clément, R. J.; Yu, X.; Leskes, M.; Pell, A. J.; Pintacuda, G.; Yang, X.-Q.; Grey, C. P.; Meng, Y. S. *Chem. Mater.* **2014**, *26* (2), 1260.

(24) Xiang, X.; Zhang, K.; Chen, J. *Adv. Mater.* **2015**, *27* (36), 5343.

(25) Hy, S.; Liu, H.; Qian, D.; Zhang, M.; Hwang, B. J.; Meng, Y. S. *Energy Environ. Sci.* **2016**, *2*, 1931.

(26) Sathiya, M.; Rousse, G.; Ramesha, K.; Laisa, C. P.; Vezin, H.; Sougrati, M. T.; Doublet, M.-L.; Foix, D.; Gonbeau, D.; Walker, W.; Prakash, A. S.; Ben Hassine, M.; Dupont, L.; Tarascon, J.-M. *Nat. Mater.* **2013**, *12* (9), 827.

(27) Ohzuku, T.; Nagayama, M.; Tsuji, K.; Ariyoshi, K. *J. Mater. Chem.* **2011**, *21* (27), 10179.

(28) Oishi, M.; Yogi, C.; Watanabe, I.; Ohta, T.; Orikasa, Y.; Uchimoto, Y.; Ogumi, Z. *J. Power Sources* **2015**, *276*, 89.

(29) Luo, K.; Roberts, M. R.; Hao, R.; Guerrini, N.; Pickup, D. M.; Liu, Y.-S.; Edström, K.; Guo, J.; Chadwick, A. V.; Duda, L. C.; Bruce, P. G. *Nat. Chem.* **2016**, *8*, 684.

(30) Seo, D.; Lee, J.; Urban, A.; Malik, R.; Kang, S.; Ceder, G. *Nat. Chem.* **2016**, *8*, 692.

(31) de la Llave, E.; Talaie, E.; Levi, E.; Nayak, P. K.; Dixit, M.; Rao, P. T.; Hartmann, P.; Chesneau, F.; Major, D. T.; Greenstein, M.; Aurbach, D.; Nazar, L. F. *Chem. Mater.* **2016**, *28* (24), 9064.

(32) Yabuuchi, N.; Hara, R.; Kajiyama, M.; Kubota, K.; Ishigaki, T.; Hoshikawa, A.; Komaba, S. *Adv. Energy Mater.* **2014**, *4* (13), 1301453.

(33) Yabuuchi, N.; Hara, R.; Kubota, K.; Paulsen, J.; Kumakura, S.; Komaba, S. *J. Mater. Chem. A* **2014**, *2* (40), 16851.

(34) Nanba, Y.; Iwao, T.; De Boisse, B. M.; Zhao, W.; Hosono, E.; Asakura, D.; Niwa, H.; Kiuchi, H.; Miyawaki, J.; Harada, Y.; Okubo, M.; Yamada, A. *Chem. Mater.* **2016**, *28* (4), 1058.

(35) Rozier, P.; Sathiya, M.; Paulraj, A. R.; Foix, D.; Desaunay, T.; Taberna, P. L.; Simon, P.; Simon, P.; Tarascon, J. M. *Electrochem. Commun.* **2015**, *53*, 29.

(36) Mortemard de Boisse, B.; Liu, G.; Ma, J.; Nishimura, S.-I.; Chung, S.-C.; Kiuchi, H.; Harada, Y.; Kikkawa, J.; Kobayashi, Y.; Okubo, M.; Yamada, A. *Nat. Commun.* **2016**, *7*, 11397.

(37) Mccalla, E.; Rowe, A. W.; Camardese, J.; Dahn, J. R. *Chem. Mater.* **2013**, *25* (13), 2716.

(38) Ender, M.; Weber, A.; Ivers-Tiffée, E. *J. Electrochem. Soc.* **2012**, *159* (2), A128.

(39) Cho, H.-M.; Meng, Y. S. *J. Electrochem. Soc.* **2013**, *160* (9), A1482.

(40) Yu, H.; Wang, Y.; Asakura, D.; Hosono, E.; Zhang, T.; Zhou, H. *RSC Adv.* **2012**, *2* (23), 8797.

(41) Xu, B.; Fell, C. R.; Chi, M.; Meng, Y. S. *Energy Environ. Sci.* **2011**, *4* (6), 2223.

(42) Lu, Z.; Dahn, J. R. *Chem. Mater.* **2001**, *13* (4), 1252.

(43) Mendiboure, A.; Delmas, C.; Hagenmuller, P. *J. Solid State Chem.* **1985**, *57* (3), 323.

(44) Clément, R. J.; Xu, J.; Middlemiss, D. S.; Alvarado, J.; Ma, C.; Meng, Y. S.; Grey, C. P. *J. Mater. Chem. A* **2017**, *5*, 4129.

(45) Yabuuchi, N.; Yoshii, K.; Myung, S.-T.; Nakai, I.; Komaba, S. *J. Am. Chem. Soc.* **2011**, *133* (12), 4404.

(46) Yu, H.; Zhou, H. *J. Phys. Chem. Lett.* **2013**, *4* (8), 1268.

(47) Wang, Z. L.; Yin, J. S.; Jiang, Y. D. *Micron* **2000**, *31* (5), 571.

(48) Qian, D.; Xu, B.; Chi, M.; Meng, Y. S. *Phys. Chem. Chem. Phys.* **2014**, *16* (28), 14665.

(49) Carroll, K. J.; Qian, D.; Fell, C.; Calvin, S.; Veith, G. M.; Chi, M.; Baggetto, L.; Meng, Y. S. *Phys. Chem. Chem. Phys.* **2013**, *15*, 11128.

(50) Armstrong, A. R.; Holzapfel, M.; Novák, P.; Johnson, C. S.; Kang, S. H.; Thackeray, M. M.; Bruce, P. G. *J. Am. Chem. Soc.* **2006**, *128* (26), 8694.

(51) Lin, F.; Nordlund, D.; Markus, I.; Weng, T.-C.; Xin, H. L.; Doeff, M. *Energy Environ. Sci.* **2014**, *7*, 3077.

(52) Yoon, W.-S.; Balasubramanian, M.; Chung, K. Y.; Yang, X.-Q.; McBreen, J.; Grey, C. P.; Fischer, D. A. *J. Am. Chem. Soc.* **2005**, *127* (1), 17479.

(53) Liu, X.; Wang, D.; Liu, G.; Srinivasan, V.; Liu, Z.; Hussain, Z.; Yang, W. *Nat. Commun.* **2013**, *4*, 2568.

(54) Soriano, L.; Gutiérrez, A.; Preda, I.; Palacín, S.; Sanz, J. M.; Abbate, M.; Trigo, J. F.; Vollmer, A.; Bressler, P. R. *Phys. Rev. B: Condens. Matter Mater. Phys.* **2006**, *74* (19), 3.

(55) Qiao, R.; Wray, L. A.; Kim, J. H.; Pieczonka, N. P. W.; Harris, S. J.; Yang, W. *J. Phys. Chem. C* **2015**, *119* (49), 27228.

(56) Jiang, M.; Key, B.; Meng, Y. S.; Grey, C. P. *Chem. Mater.* **2009**, *21* (13), 2733.

(57) Oishi, M.; Fujimoto, T.; Takanashi, Y.; Orikasa, Y.; Kawamura, A.; Ina, T.; Yamashige, H.; Takamatsu, D.; Sato, K.; Murayama, H.; Tanida, H.; Arai, H.; Ishii, H.; Yogi, C.; Watanabe, I.; Ohta, T.; Mineshige, A.; Uchimoto, Y.; Ogumi, Z. *J. Power Sources* **2013**, *222*, 45.

(58) Hy, S.; Su, W.-N.; Chen, J.-M.; Hwang, B.-J. *J. Phys. Chem. C* **2012**, *116* (48), 25242.

(59) De Groot, F. M. F.; Grioni, M.; Fuggle, J. C.; Ghijsen, J.; Sawatzky, G. A.; Petersen, H. *Phys. Rev. B: Condens. Matter Mater. Phys.* **1989**, *40* (8), 5715.

(60) Qiao, R.; Chuang, Y. De; Yan, S.; Yang, W. *PLoS One* **2012**, *7* (11), 3.

(61) Yabuuchi, N.; Kajiyama, M.; Iwatate, J.; Nishikawa, H.; Hitomi, S.; Okuyama, R.; Usui, R.; Yamada, Y.; Komaba, S. *Nat. Mater.* **2012**, *11* (6), 512.